High-Res Brain Source Imaging of MEG using a Vector Bayesian Beamformer with Noise learning

Tianyu Gao[1], Kunye Liu[1], Weikai Ma[1], Yang Gao[1,2(✉)], and Xiaolin Ning[1,2(✉)]

[1] School of Instrumentation Science and Optoelectronic Engineering, Beihang University, Beijing 100191, China
[2] Hefei National Laboratory, Hefei 230088,China
yanggao@buaa.edu.cn
ningxiaolin@buaa.edu.cn

Abstract. Magnetoencephalogram (MEG) with high spatio-temporal resolution plays a crucial role in the field of functional imaging. Incorporating vector source modeling enables explicit estimation of triaxial current components, thereby mitigating reconstruction errors caused by orientation bias in scalar leadfield approximations. This directional precision enables accurate identification of epileptogenic zones and oscillatory network hubs, providing neurosurgeons with electrophysiologically validated targets. Vector beamformers, grounded in spatial filtering theory, provide computationally efficient solutions for large-scale sensor data and dynamic high-resolution analyses. However, a vector source requires a vector beamformer whose performance degrades under high noise, limited time samples, or strongly correlated sources due to sample covariance matrix singularity. In this study, we propose a vector Bayesian learning framework to enhance beamformer robustness by addressing covariance matrix singularity. Specifically, we model the vector source linear system with full positive-definite noise covariance structures and employ data-driven Bayesian learning to refine the sample covariance matrix. By leveraging sparsity priors on source distributions and data-driven, our method improves spatial focusing and temporal reconstruction accuracy. We validated the approach using simulated data across varying signal-to-noise ratios (SNR) and real 64-channel optically pumped magnetometer (OPM)-MEG datasets under diverse stimulus-evoked paradigms. Comparative evaluations demonstrate that our Bayesian learning-based framework achieves 18. 03% higher AUC compared to conventional beamformers while preserving millimeter-level spatial precision, outperforming existing benchmarks in both spatial localization accuracy and dynamic reconstruction fidelity for neuroscience and clinical applications. Our codes are publicly accessible at: https://github.com/gao815/VBNLBF.

Keywords: Inverse problem · Beamformer · Bayesian learning · MEG.

1 Introduction

Magnetoencephalography (MEG) offers unparalleled spatiotemporal resolution for mapping neural dynamics and clinical diagnostics. The core advantage of MEG compared to electroencephalography (EEG) and techniques such as functional magnetic resonance imaging (fMRI) lies in its ability to directly capture the vector properties (direction and strength) of neural currents. This enables more precise localization in source reconstruction, overcoming the directional ambiguity inherent in EEG (due to volume conductor effects) and indirect neural activity measurements of fMRI [1,2,3]. Despite these technological divergences, both modalities fundamentally require precise neural source localization for functional interpretation. This critical dependency underscores the importance of brain source imaging (BSI), which enables neural activity reconstruction and real-time neurofeedback synchronization essential for closed-loop neuromodulation therapies. However, the electromagnetic inverse problem's inherent ill-posedness, where infinite dipole configurations yield identical magnetic field measurements - necessitates mathematical frameworks integrating neuroanatomical constraints [4]. This challenge motivated the adaptation of beamforming techniques from radar signal processing to BSI [5,7]. Through spatial filtering principles, these methods selectively amplify target neural signals while suppressing interference from noise sources.

Distributed models map brain activity via voxel-grid dipoles with directional strength. Because the true direction of the source cannot be obtained, the scalar leadfield cannot be accurately reconstructed. Cortically constrained scalar models typically fix dipole orientations perpendicular to the cortical surface, aligning with pyramidal neuron geometry [8]. However, this assumption fails for subcortical sources lacking laminar organization and dynamic scenarios involving orientation shifts. Although vector-based models outperform scalar approaches in neurophysiological fidelity, they triple parameter dimensionality compared with case of fixed direction, intensifying the inverse problem's ill-posedness, motivating beamformers that inherently estimate orientation vector via spatial covariance analysis.

Beamforming techniques employ adaptive spatial filters to amplify target signals while suppressing interference. The minimum variance distortionless response (MVDR) beamformer [9] and anatomically constrained variants [10,11,12] provide computational efficiency and millimeter spatial resolution, ideal for the whole-brain vector source reconstruction. Notably, conventional beamformers face two limitations (Fig. 1(a)): (1) Singularity in sample covariance matrices under finite time samples or correlated sources, typically mitigated via diagonal loading or projection schemes (e.g., synchronous abnormal discharge activity in epilepsy [6] or event-related activity in primary sensory areas); (2) Covariance estimation bias in low-signal noise ratio (SNR) regimes with limited samples, violating asymptotic consistency assumptions [11]. Furthermore, sparse Bayesian frameworks [13,14,15] enhance non-adaptive methods like weighted minimum norm estimation (wMNE) [16] through data-driven priors, yet suffer from sensitivity loss in high-dimensional spaces, reconstructed images exhibit excessive

sparsity and computational inefficiency for real-time applications. A hybrid approach integrating data-driven methodologies with beamforming techniques may serve as a promising strategy for achieving high-resolution neural source imaging.

To overcome these challenges, we propose VBNLBF: a vector Bayesian beamformer with noise learning. Proposed method integrates three innovations: (1) Hierarchical priors jointly regularizing source and noise spaces to estimate data covariance and enhance the noise robustness; (2) Grounded positive-definite noise modeling to solve the singularity covariance problem of the correlated source; (3) A convex update optimization enabling vector reconstruction. Evaluated on synthetic benchmarks (-5-10 dB SNR) and 64-channel OPM-MEG data, this method achieves 18. 03% higher AUC compared to conventional beamformers while maintaining millimeter-level spatial precision. Critically, it resolves correlated source pairs unmanageable by existing methods, establishing clinical-grade localization accuracy.

2 Methods and Vectorized Interpretation

2.1 Bayesian modeling of source and positive definite noise model

MEG measurements and neural source activity admit a linear hierarchical priors representation: $\boldsymbol{B} = \boldsymbol{L}\boldsymbol{S} + \boldsymbol{\varepsilon}$, where $\boldsymbol{B} \in \mathbb{R}^{d_b \times d_T}$ denotes sensor signals from d_b channels over d_T time samples. The source matrix $\boldsymbol{S} \in \mathbb{R}^{3d_s \times d_T}$ encodes 3D current distributions for d_s neural sources, with each source $\boldsymbol{s}_i = [\boldsymbol{s}_i^x, \boldsymbol{s}_i^y, \boldsymbol{s}_i^z]^T \in \mathbb{R}^{3 \times d_T}$ representing vectorial dipole moments. Here, the leadfield matrix $\boldsymbol{L} \in \mathbb{R}^{d_b \times 3d_s}$ contains three orthogonal components $\boldsymbol{L}_i = [\boldsymbol{L}_i^x, \boldsymbol{L}_i^y, \boldsymbol{L}_i^z]$ per source, mapping cortical currents to sensor space. Additive noise $\boldsymbol{\varepsilon} \in \mathbb{R}^{d_b \times d_T}$ exhibits temporal independence and identical distribution. Notably, Maxwell's quasi-static approximation renders MEG more sensitive to tangential than radial cortical sources, while the leadfield's ill-conditioning amplifies radial noise [4]. To ensure numerical stability, we applied rank projection to $\boldsymbol{L}$ during forward model construction. Although our framework employs full 3D current components for comprehensive vector source modeling, it remains compatible with lower-dimensional configurations. As Fig. 1(b) illustrates, we formalize the variable distribution relationship through a hierarchical Bayesian Gaussian model derived from the general linear framework: $p(\boldsymbol{B}|\boldsymbol{S}) = \prod_{t=1}^{d_T} \mathcal{N}(\boldsymbol{L}\boldsymbol{s}^t, \boldsymbol{\Sigma}_n)$, $p(\boldsymbol{S}) = \prod_{t=1}^{d_T} \mathcal{N}(\boldsymbol{0}, \boldsymbol{\Sigma}_s)$, and $p(\boldsymbol{\varepsilon}) = \prod_{t=1}^{d_T} \mathcal{N}(\boldsymbol{0}, \boldsymbol{\Sigma}_n)$. The variables $\boldsymbol{B}$, $\boldsymbol{S}$, and $\boldsymbol{\varepsilon}$ are temporally independent and identically distributed. Traditional diagonal covariance assumptions $\boldsymbol{\Sigma}_s^i = \mathrm{diag}\left(\sigma_{ix}^2, \sigma_{iy}^2, \sigma_{iz}^2\right)$ enforce component-wise independence, causing biased axial estimates. We instead propose a block-diagonal structure: $\boldsymbol{\Sigma}_s = \mathrm{diag}\left(\boldsymbol{\Sigma}_{s_1}, \cdots, \boldsymbol{\Sigma}_{s_{d_s}}\right), \quad \boldsymbol{\Sigma}_s^i \succeq 0$, where $\boldsymbol{\Sigma}_{s_i}$ is a 3×3 positive semi-definite matrix modeling ellipsoidal covariation. The trace $tr(\boldsymbol{\Sigma}_{s_i})$ regulates source strength, providing a differentiable foundation for optimization.

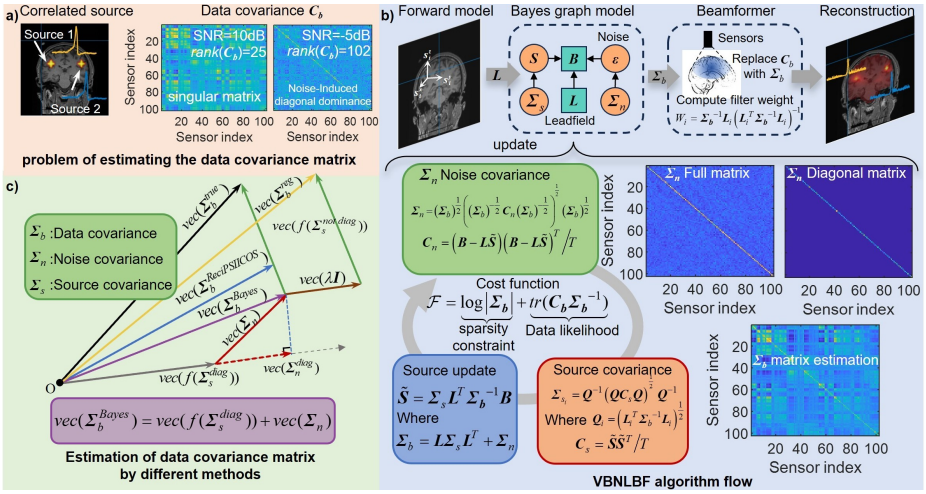

Fig. 1. The beamformer problem and matrix update methods in magnetoencephalography source imaging, along with the VBNLBF algorithm process. a) Problem of estimating the data covariance matrix; b) VBNLBF algorithm flow; c) Vectorized interpretation of different methods.

Adopting Bayesian learning [17], we reword BSI as marginal likelihood optimization: $\boldsymbol{\Theta} = \arg\max_{\boldsymbol{\Theta}} p(\boldsymbol{B}|\boldsymbol{\Sigma}_b) = \arg\max_{\boldsymbol{\Theta}} \int p(\boldsymbol{B}|\boldsymbol{S}, \boldsymbol{\Sigma}_n)\, p(\boldsymbol{S}|\boldsymbol{\Sigma}_s)\, d\boldsymbol{S}$, where $\boldsymbol{\Theta} = \{\boldsymbol{\Sigma}_s, \boldsymbol{\Sigma}_n\}$ and $\boldsymbol{\Sigma}_b = \boldsymbol{L}\boldsymbol{\Sigma}_s\boldsymbol{L}^T + \boldsymbol{\Sigma}_n$. Negative log-likelihood becomes:

$$\mathcal{F} = \log|\boldsymbol{\Sigma}_b| + tr\left(\boldsymbol{C}_b\boldsymbol{\Sigma}_b^{-1}\right), \tag{1}$$

with $\boldsymbol{C}_b = \frac{1}{d_T}\boldsymbol{B}\boldsymbol{B}^T$. The former enforces sparsity; the latter ensures fidelity.

Using convex geometry optimization [18,14,15], we develop a convex update strategy to surpass Expectation Maximization (EM) algorithm limitations. Updates alternate between $\boldsymbol{\Sigma}_s$, $\boldsymbol{\Sigma}_n$, and $\tilde{\boldsymbol{S}}$, constrained to their respective manifolds. Since $\log|\boldsymbol{\Sigma}_b|$ is concave in $\boldsymbol{\Sigma}_{s_i}$, we introduce 3×3 auxiliary variables $\boldsymbol{V}_i \succ 0$ to construct a convex upper bound [18]: $\tilde{\mathcal{F}} = tr\left(\boldsymbol{C}_b\boldsymbol{\Sigma}_b^{-1}\right) + \sum_{i=1}^{d_s} tr\left(\boldsymbol{V}_i^T\boldsymbol{\Sigma}_{s_i}\right) + v_0$, where v_0 is a scalar intercept. Solving $\partial\tilde{\mathcal{F}}/\partial\boldsymbol{\Sigma}_{s_i} = 0$ yields:

$$\boldsymbol{V}_i = \boldsymbol{L}_i^T\boldsymbol{\Sigma}_b^{-1}\boldsymbol{L}_i, \quad \boldsymbol{\Sigma}_{s_i} = \boldsymbol{V}_i^{-\frac{1}{2}}\left(\boldsymbol{V}_i^{\frac{1}{2}}\boldsymbol{C}_s\boldsymbol{V}_i^{\frac{1}{2}}\right)^{\frac{1}{2}}\boldsymbol{V}_i^{-\frac{1}{2}}, \tag{2}$$

with $\boldsymbol{L}_i$ denotes the i-th column vector of matrix $\boldsymbol{L}$ and $\boldsymbol{C}_s = \frac{1}{d_T}\tilde{\boldsymbol{S}}\tilde{\boldsymbol{S}}^T$. Given $\boldsymbol{\Sigma}_s^i \succeq 0$ and $\boldsymbol{\Sigma}_n \succ 0$, the minimum eigenvalue of $\boldsymbol{\Sigma}_b$ satisfies $\lambda_{\min}(\boldsymbol{\Sigma}_b) \geq \lambda_{\min}(\boldsymbol{\Sigma}_n) > 0$, ensuring strict positive definiteness. Grounded noise covariance updates on the symmetric positive-definite (PD) manifold [14] can effectively solve the singularity of covariance matrix. Eq. 1 can be restated as:

$$\mathcal{F}\left(\boldsymbol{\Sigma}_n\right) = tr\left(\boldsymbol{\Sigma}_b^{-1}\boldsymbol{\Sigma}_n\right) + tr\left(\boldsymbol{C}_n\boldsymbol{\Sigma}_n^{-1}\right), \tag{3}$$

with $\boldsymbol{C}_n = \frac{1}{d_T}(\boldsymbol{B} - \boldsymbol{L}\tilde{\boldsymbol{S}})(\boldsymbol{B} - \boldsymbol{L}\tilde{\boldsymbol{S}})^T$. In the same way, $\boldsymbol{\Sigma}_n$ updates are:

$$\boldsymbol{\Sigma}_n = \boldsymbol{\Sigma}_b^{\frac{1}{2}}\left(\boldsymbol{\Sigma}_b^{-\frac{1}{2}}\boldsymbol{C}_n\boldsymbol{\Sigma}_b^{-\frac{1}{2}}\right)^{\frac{1}{2}}\boldsymbol{\Sigma}_b^{\frac{1}{2}}. \tag{4}$$

Posterior expectation of $\tilde{\boldsymbol{S}}$ updates as:

$$\tilde{\boldsymbol{S}} = \boldsymbol{\Sigma}_s\boldsymbol{L}^T\boldsymbol{\Sigma}_b^{-1}\boldsymbol{B}. \tag{5}$$

Use Eq. (2) (4) (5) to alternately update variables until the change in less than the objective function $\mathcal{F}$ is less than the set tolerance δ, and output the data covariance $\boldsymbol{\Sigma}_b$ estimation for the current iteration as input to the beamformer.

2.2 Beamforming reconstruction

The vector beamformer [18] reconstructs source activity using the updated $\boldsymbol{\Sigma}_b$. For the i-th neural source, the spatial filter solution is derived as:

$$\boldsymbol{W}_i = \boldsymbol{\Sigma}_b^{-1}\boldsymbol{L}_i\left(\boldsymbol{L}_i^T\boldsymbol{\Sigma}_b^{-1}\boldsymbol{L}_i\right)^{-1}, \tag{6}$$

yielding the estimated source activity $\boldsymbol{S}_i$ and activation power $\boldsymbol{P}_i$:

$$\boldsymbol{S}_i = \boldsymbol{W}_i^T\boldsymbol{B}, \quad \boldsymbol{P}_i = \sqrt{\left(\boldsymbol{S}_{i,x}\right)^2 + \left(\boldsymbol{S}_{i,y}\right)^2 + \left(\boldsymbol{S}_{i,z}\right)^2}. \tag{7}$$

2.3 Vectorized interpretation

The performance limitations of beamformers originate from perturbations induced by off-diagonal elements in $\boldsymbol{\Sigma}_b$, formally expressed as [19]:

$$\boldsymbol{W}_i^T\boldsymbol{B} = \boldsymbol{S}_i^{true} + \sum_{j\neq i}\boldsymbol{S}_j^{true}\frac{(\boldsymbol{\Sigma}_b^{-1})_{ij}}{(\boldsymbol{\Sigma}_b^{-1})_{ii}}, \tag{8}$$

where the second term quantifies leakage contributions from correlated source covariance. Vectorization of $\boldsymbol{\Sigma}_b$ elucidates beamformer mechanisms [11]: $\mathrm{vec}(\boldsymbol{\Sigma}_b) = \sum_{i=1}^{d_s}\mathrm{vec}\left(\boldsymbol{L}_i\boldsymbol{L}_i^T(\boldsymbol{\Sigma}_s)_{ii}\right) + \sum_{i=1}^{d_s}\sum_{j>i}\mathrm{vec}\left((\boldsymbol{L}_j\boldsymbol{L}_i^T + \boldsymbol{L}_i\boldsymbol{L}_j^T)(\boldsymbol{\Sigma}_s)_{ij}\right) + \mathrm{vec}(\boldsymbol{\Sigma}_n)$, partitioned into diagonal source terms ($\mathrm{vec}(f(\boldsymbol{\Sigma}_s^{\mathrm{diag}}))$), off-diagonal coupling terms ($\mathrm{vec}(f(\boldsymbol{\Sigma}_s^{\mathrm{off-diag}}))$), and noise. Spatial sparsity priors enforce $\mathrm{rank}(\boldsymbol{\Sigma}_s) \ll d_s$, with little sparse dominant diagonal entries $(\boldsymbol{\Sigma}_s)_{ii} \gg 0$. As Fig. 1(c) illustrates, Conventional diagonal loading [9], $\boldsymbol{\Sigma}_b \leftarrow \boldsymbol{\Sigma}_b + \lambda\boldsymbol{I}$, preserves $\boldsymbol{\Sigma}_s^{\mathrm{diag}}$ structure under moderate SNR but requires careful λ tuning and fails to address $(\boldsymbol{\Sigma}_b^{-1})_{ij}$ effects. Advanced methods (e.g., ReciPSIICOS [11,19]) suppress these terms via projections. Under low-SNR white noise, $\boldsymbol{\Sigma}_b$ retains full rank but noise dominance biases diagonal ratios $\left(\boldsymbol{\Sigma}_b^{\mathrm{clean}}\right)_{ii} \Big/ \left(\left(\boldsymbol{\Sigma}_b^{\mathrm{clean}}\right)_{ii} + (\boldsymbol{\Sigma}_n)_{ii}\right)$,

impairing noise suppression. Our Bayesian framework jointly learns $\boldsymbol{\Sigma}_n$ (positive definite) and $\boldsymbol{\Sigma}_s^{\text{diag}}$, eliminating $\text{vec}(f(\boldsymbol{\Sigma}_s^{\text{off}-\text{diag}}))$ interference to enhance robustness against correlated sources and noise.

3 Experiment

To evaluate the proposed method, we compared VBNLBF against three benchmark categories: (1) Norm-constrained methods: weighted minimum norm estimate (wMNE) [16] and standardized low-resolution electromagnetic tomography (sLORETA) [20]; (2) Covariance-optimized methods: regularized linear constrained minimum variance beamformer (LCMV) [8], Bayesian principal component analysis beamformer (bPCA-LCMV) [10], and spatial projector ReciPSIICOS [11]; (3) Bayesian frameworks: Champagne-NL [18] (accurate scalar leadfield) and Bayesian learning beamformer (BLBF) [13] (single-axis scalar leadfield). All methods employed normalized leadfields.

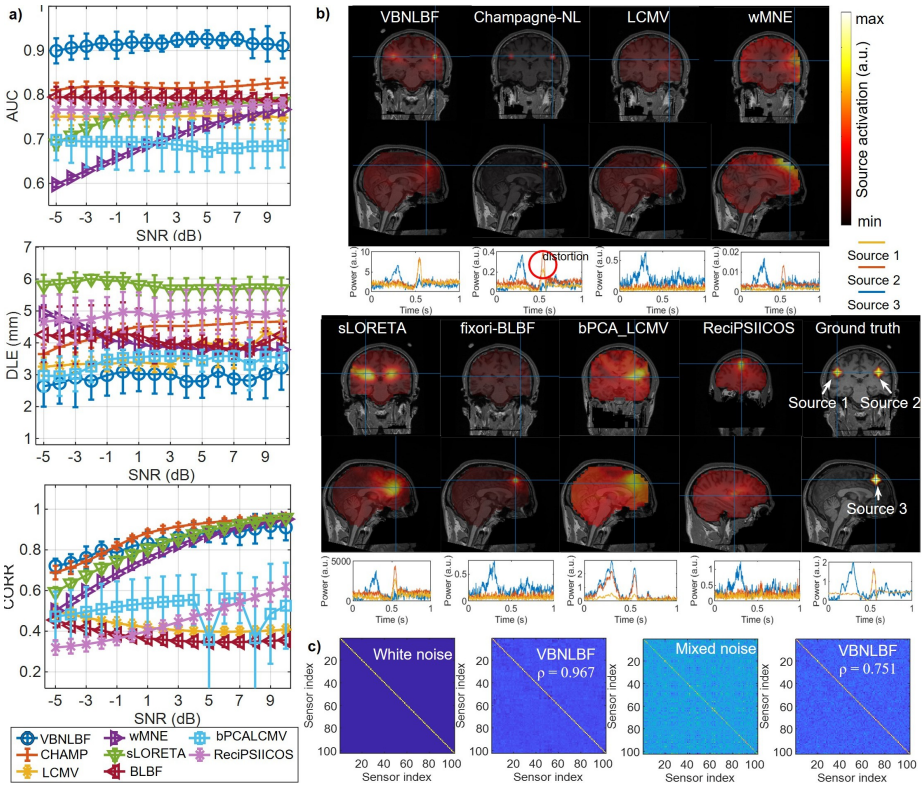

Fig. 2. Performance metrics of reconstruction algorithms in simulated source scenarios. a) Evaluation metrics at different SNR; b) Source and waveform reconstruction under SNR = 5dB. c) Noise covariance estimation under different noise types.

We simulated three neural sources using a 102-channel MEG single-shell head model [21] with 8 mm grid resolution: two correlated bilateral temporal sources (synchronized time courses) and one independent source. Neural mass models (NMM) [22] generated activation waveforms with additive correlated noise (SNR: -5-10 dB). Each configuration underwent 20 Monte Carlo trials. We evaluated: 1) Spatial accuracy: Dipole localization error (DLE). 2) Reconstruction reliability: Area under curve (AUC). 3) Temporal fidelity: Correlation coefficient (Corr). Ground truth refers to the activation strength and location of the simulation source setting under noise-free conditions. The calculation details for each evaluation index can be found in the supplementary file in github.

Simulations were conducted on a 13th Gen Intel Core i9-13900HX processor at 2.20 GHz. The inference process typically required 200–500 iterations to converge, with a total runtime under ten minutes for the simulations presented in this study. The primary computational bottleneck lies in covariance matrix inversion operations, whose complexity increases with d_s and d_b. Thus, the proposed method is more suitable for high-precision offline analysis.

Table 1. Performance metrics of algorithm across noise configurations. (Mean±Std)

method	AUC	DLE(mm)
VBNLBF	**0.9162±0.0233**	**2.9248±0.6218**
CHAMP	0.8180±0.0114	4.3635±0.1981
LCMV	0.7511±0.0236	3.1487±0.3824
wMNE	0.6932±0.0099	4.0775±0.2144
sLORETA	0.7565±0.0082	5.7931±0.3148
BLBF	0.7925±0.0189	4.0977±0.6374
bPCALCMV	0.6885±0.0561	3.4005±0.3485
ReciPSIICOS	0.7695±0.0166	4.8694±0.7003

Under low SNR (SNR $<$ 0 dB), VBNLBF achieved significantly higher AUC (0.9089 ± 0.0260) and Corr (0.7603 ± 0.0488) than other methods, with comparable DLE (Fig. 2(a)). Traditional LCMV and BLBF exhibited SNR-correlated performance decline (e.g., LCMV Corr decreased from 0.4991 to 0.4081) due to $>$70% amplitude attenuation in correlated sources. VBNLBF improved AUC by 18.03%, resolving correlated source confusion and noise sensitivity matching for LCMV (1). In contrast, VBNLBF maintained low localization error within one voxel (DLE $<$ 4 mm) and reconstruct sources 1 and 2 wavelet amplitudes via Bayesian hierarchical modeling compared with CHAMP's oversparse solutions under accurate lead direction (Fig. 2(b)), which also shows that the spatial filter built by beamforming improves the situation where the source is too sparse due to Bayesian frame focusing. In addition, we evaluated VBNLBF under 5 dB mixed correlated noise and white noise. Under different noise environment, VBNLBF algorithm can learn the intrinsic information of noise. Cosine similarity analysis (Fig. 2(c)) corroborated this ($\rho_{\text{mixed}} = 0.751, \rho_{\text{white}} = 0.967$). This highlights Bayesian full noise covariance structure learning's adaptability,

though the positive definite covariance's off-diagonal elements may introduce minor $\boldsymbol{\Sigma}_b^{-1}$-based spatial weighting errors (Eq. 8), slightly degrading resolution in positive definite noise covariance regimes with high SNR. Overall, the performance of our algorithm is optimal in different noise environments and correlated source configurations.

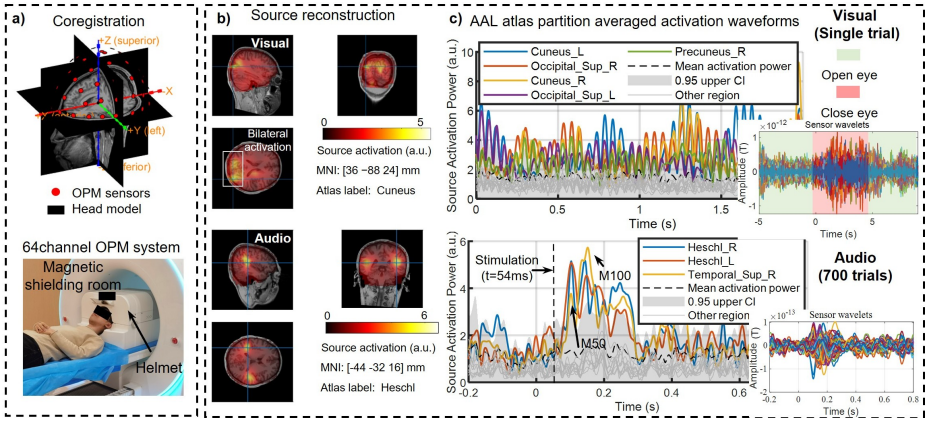

Fig. 3. Brain magnetoencephalographic source reconstruction and stimulation response analysis based on OPM-MEG, with corresponding time series waveforms. a) Coregistration result and OPM-MEG device; b) Source reconstruction imaging results; c) AAL atlas partition [23] averaged activation waveforms.

Two kinds of validation experiment utilized 64-channel OPM-MEG recordings from three adults (24±2 years) in a magnetically shielded room (Fig. 3(a)). Individual head models employed 8 mm MNI-standard source space coregistration with single-shell forward modeling [21]. For single trial eyes-closed visual tasks (Fig. 3(b)), VBNLBF reconstructed alpha-band (8-13 Hz) bilateral occipital activations under low SNR, with global field power analysis revealing significant activity in cuneus (Cuneus L/R) and superior occipital gyrus (Occipital-Sup L/R) [23,24], exceeding 95% baseline confidence intervals. Peak activation (MNI:36 -88 24) localized to visual cortex [24,25]. In correlated auditory paradigms (700 pure-tone stimuli), VBNLBF identified bilateral Heschl's gyrus activations (MNI:-44 -32 16), reconstructing correlated characteristic M50/M100 evoked components in temporal regions, consistent with established neurophysiological patterns [26,27].

4 Conclusion

While the VBNLBF introduces computational demands due to its rigorous covariance estimation framework — particularly the super-linear complexity scaling with source space grid density, Accurate covariance estimation can resolve

performance limitations of conventional methods in low-SNR, correlated source, and uncertain noise covariance regimes. By jointly optimizing block-diagonal source covariance and positive-definite noise structures, our framework adaptively regularizes covariance degeneration while enhancing noise robustness. Experimental validation demonstrates that VBNLBF achieves an 18.03% improvement in AUC compared to conventional LCMV, establishing this non-invasive technique as a robust clinical solution for overcoming resolution limitations in synchronous epileptogenic foci discrimination and guiding precise resection surgery.

5 Disclosure of Interests

The authors declare that they have no known competing financial interests or personal relationships that could have appeared to influence the work reported in this paper.

References

1. Boto, E., Holmes, N., Leggett, J., Roberts, G., Shah, V., Meyer, S.S., et al.: Moving magnetoencephalography towards real-world applications with a wearable system. Nature **555**(7698), 657–661 (2018)
2. Brookes, M.J., Leggett, J., Rea, M., Hill, R.M., Holmes, N., Boto, E., et al.: Magnetoencephalography with optically pumped magnetometers (OPM-MEG): the next generation of functional neuroimaging. Trends in Neurosciences **45**(8), 621–634 (2022)
3. Beltrachini, L., et al.: Optimal design of on-scalp electromagnetic sensor arrays for brain source localisation. Human Brain Mapping **42**(15), 4869–4879 (2021)
4. Sekihara, K., Nagarajan, S.S.: Electromagnetic Brain Imaging: A Bayesian Perspective. Springer International Publishing, Cham (2015)
5. Wan, F., Xu, J., Zhang, Z.: Robust Beamforming Based on Covariance Matrix Reconstruction in FDA-MIMO Radar to Suppress Deceptive Jamming. Sensors **22**(4), 1479 (2022)
6. Carrette, E., Stefan, H.: Evidence for the Role of Magnetic Source Imaging in the Presurgical Evaluation of Refractory Epilepsy Patients. Frontiers in Neurology **10**, 933 (2019)
7. Rosado-Sanz, J., Jarabo-Amores, M.P., De La Mata-Moya, D., Rey-Maestre, N.: Adaptive Beamforming Approaches to Improve Passive Radar Performance in Sea and Wind Farms' Clutter. Sensors **22**(18), 6865 (2022)
8. Fuchs, M., Kastner, J., Tech, R., Wagner, M., Gasca, F.: MEG and EEG dipole clusters from extended cortical sources. Biomedical Engineering Letters **7**(3), 185–191 (2017)
9. Van Veen, B.D., Van Drongelen, W., Yuchtman, M., Suzuki, A.: Localization of brain electrical activity via linearly constrained minimum variance spatial filtering. IEEE Transactions on Biomedical Engineering **44**(9), 867–880 (1997)
10. Woolrich, M., Hunt, L., Groves, A., Barnes, G.: MEG beamforming using Bayesian PCA for adaptive data covariance matrix regularization. NeuroImage **57**(4), 1466–1479 (2011)

11. Kuznetsova, A., Nurislamova, Y., Ossadtchi, A.: Modified covariance beamformer for solving MEG inverse problem in the environment with correlated sources. NeuroImage **228**, 117677 (2021)
12. Samadzadehaghdam, N., Makkiabadi, B., Masjoodi, S., Mohammadi, M., Mohagheghian, F.: A new linearly constrained minimum variance beamformer for reconstructing EEG sparse sources. International Journal of Imaging Systems and Technology **29**(4), 686–700 (2019)
13. Cai, C., Long, Y., Ghosh, S., Hashemi, A., Gao, Y., Diwakar, M., et al.: Bayesian Adaptive Beamformer for Robust Electromagnetic Brain Imaging of Correlated Sources in High Spatial Resolution. IEEE Transactions on Medical Imaging **42**(9), 2502–2512 (2023)
14. Hashemi, A., Cai, C., Gao, Y., Ghosh, S., Müller, K.-R., Nagarajan, S.S., et al.: Joint Learning of Full-Structure Noise in Hierarchical Bayesian Regression Models. IEEE Transactions on Medical Imaging **43**(2), 610–624 (2024)
15. Westner, B.U., Dalal, S.S., Gramfort, A., Litvak, V., Mosher, J.C., Oostenveld, R., et al.: A unified view on beamformers for M/EEG source reconstruction. NeuroImage **246**, 118789 (2022)
16. Lin, F.-H., Witzel, T., Ahlfors, S.P., Stufflebeam, S.M., Belliveau, J.W., Hämäläinen, M.S.: Assessing and improving the spatial accuracy in MEG source localization by depth-weighted minimum-norm estimates. NeuroImage **31**(1), 160–171 (2006)
17. Wu, W., Nagarajan, S., Chen, Z.: Bayesian Machine Learning: EEG/MEG signal processing measurements. IEEE Signal Processing Magazine **33**(1), 14–36 (2016)
18. Cai, C., Kang, H., Hashemi, A., Chen, D., Diwakar, M., Haufe, S., et al.: Bayesian Algorithms for Joint Estimation of Brain Activity and Noise in Electromagnetic Imaging. IEEE Transactions on Medical Imaging **42**(3), 762–773 (2023)
19. Ossadtchi, A., Altukhov, D., Jerbi, K.: Phase shift invariant imaging of coherent sources (PSIICOS) from MEG data. NeuroImage **183**, 950–971 (2018)
20. Pascual-Marqui, R.D.: Standardized low-resolution brain electromagnetic tomography (sLORETA): technical details. Methods and Findings in Experimental and Clinical Pharmacology **24**(Suppl. D), 5–12 (2002)
21. Malmivuo, J., Plonsey, R.: Bioelectromagnetism Principles and Applications of Bioelectric and Biomagnetic Fields. Oxford University Press, Oxford (1995)
22. Lopez-Sola, E., Sanchez-Todo, R., Lleal, È., Köksal-Ersöz, E., Yochum, M., Makhalova, J., et al.: A personalizable autonomous neural mass model of epileptic seizures. Journal of Neural Engineering **19**(5), 055002 (2022)
23. Rolls, E.T., Huang, C.-C., Lin, C.-P., Feng, J., Joliot, M.: Automated anatomical labelling atlas 3. NeuroImage **206**, 116189 (2020)
24. Ciulla, C., Takeda, T., Endo, H.: MEG Characterization of Spontaneous Alpha Rhythm in the Human Brain. Brain Topography **11**(3), 211–222 (1999)
25. Petro, N.M., Ott, L.R., Penhale, S.H., Rempe, M.P., Embury, C.M., Picci, G., et al.: Eyes-closed versus eyes-open differences in spontaneous neural dynamics during development. NeuroImage **258**, 119337 (2022)
26. Roberts, T.P., Poeppel, D.: Latency of auditory evoked M100 as a function of tone frequency. NeuroReport **7**(6), 1138–1140 (1996)
27. Iyer, D., Díaz, J., Zouridakis, G.: Consistency of the auditory evoked response: The presence of aberrant responses and their effect on N100 localization. Journal of Neuroscience Methods **208**(2), 173–180 (2012)